Characterization of highly dispersed Ni/Al$_2$O$_3$ catalysts by EXAFS analysis of higher shells

Takafumi Shido [a,*], Martin Lok [b] and Roel Prins [a,**]

[a] *Laboratory for Technical Chemistry, Swiss Federal Institute of Technology (ETH), 8092 Zürich, Switzerland*
E-mail: prins@tech.chem.ethz.ch
[b] *Synetix, Cleveland TS23 1LB, UK*

The size and morphology of Ni/Al$_2$O$_3$ catalysts in the oxidic, reduced, and passivated state were determined by EXAFS analysis of the higher shells around the Ni atoms. In the oxidic state, the Ni cations were present in small NiO$_x$ particles with predominant (111) plane. Below 4.5 wt% Ni loading, the NiO$_x$ particles consisted of one Ni layer, and of two or three Ni layers above 4.5 wt% Ni. A Ni–Al contribution was observed in samples with low Ni loading. The layer which is in contact with the Al$_2$O$_3$ surface is affected by the support surface and its structure is highly distorted, while the other layers were not distorted and have a structure similar to that in bulk NiO. In the reduced state, the number of Ni metal atoms in the reduced Ni particles was smaller than 100 with a narrow distribution below a loading of 15.6 wt% Ni. Above this loading, the particle size suddenly increased and the distribution became wider. The distances and Debye–Waller factors were similar to those of bulk nickel which suggested a weak interaction between the particles and the support. In the passivated state, Ni kernels with 20–40 metal atoms were covered by a one layer thick NiO skin.

Keywords: Ni, θ-alumina, EXAFS, passivated

1. Introduction

Alumina-supported nickel catalysts are used in the hydrogenation of olefins and aromatics and in the saturation of commercial solvents. A new range of such metal catalysts, the so-called HTC catalysts, has been developed [1] which possess a high specific nickel surface area as well as a high reducibility. This combination of high nickel dispersion and very low but effective metal–support interaction raised questions about the nature of the stabilisation of the metal particles onto the support. To answer these questions, extended X-ray fine structure (EXAFS) at Ni K-edge was measured of the catalysts in the oxidic, reduced and passivated states. The higher shell as well as the first shell contributions of the EXAFS spectra were analysed to investigate the morphology of the supported nickel particles.

EXAFS has been widely used to investigate the structure of supported catalysts [2–4]. It is the only method to investigate the local structures of non-crystalline materials under arbitrary atmospheric, temperature, and pressure conditions. One of the weak points of EXAFS was that quantitatively analysis of higher shells was almost impossible because the multiple scattering theory was not developed well enough. The multiple scattering contributions of the first shell, which overlap higher shell contributions should be subtracted from a Fourier-transformed or Fourier-filtered EXAFS function to elucidate the structural parameters of the higher shell contributions. An EXAFS theory which takes multiple scattering into account, however, has recently been developed by Rehr and Albert [5] and the computer program "FEFF5" and higher versions are now available to simulate EXAFS functions taking multiple scattering into account. The agreement between the calculated and observed EXAFS functions is excellent if the central atom is an element in the first row of the periodic table, such as Fe, Co and Ni [6,7].

With the aid of quantitative higher shell analysis, information of the morphology and size of catalyst particles as well as that of the local structure can be obtained. In the case of oxide and sulphide catalysts, little information of morphology is included in the first shell Metal(M)–O, or M–S contribution because the coordination numbers (CN's) are equal to that of bulk oxide or sulphide in many cases [8–10]. Such information can be contained in the M–M contributions of higher shells. The morphology of the oxide and sulphide particles can be estimated from the CN's of the M–M contributions. In the case of metal catalysts, the CN of the first shell is almost insensitive to the particle size above a certain size of particle (ca. 200 metal atoms, M$_{200}$) [11–14]. By contrast, the CN's of the higher shells are more sensitive. Hence it may be possible to determine the particle size from the higher shell contributions more accurately. In addition, the morphology of the particle and/or the particle size distribution may be obtained from the CN's of several contributions.

2. Experimental

2.1. Samples

Catalyst samples were prepared by pore volume impregnation of a transition alumina support, followed by drying

---

* Present address: Department of Chemistry, The University of Tokyo, Hongo, Bunkyo-ku, Tokyo 113, Japan.
** To whom correspondence should be addressed.

Table 1
Ni loadings and surface areas of the Ni catalysts.

Code	Ni loading (wt%)	Ni surface area (m²/g-Ni)[a]
Oxidic catalyst		
HTC-1.9(ox)	1.9	170
HTC-4.5(ox)	4.5	193
HTC-100(ox)	7.8	161
HTC-200(ox)	12.5	146
HTC-400(ox)	15.6	165
HTC-500(ox)	18.6	167
Reduced and passivated		
HTC-100(p)	9.4	137
HTC-200(p)	13.0	157
HTC-400(p)	15.5	140
HTC-500(p)	19.0	141

[a] Estimated by static hydrogen chemisorption following reduction of the oxidic catalysts assuming that one Ni atom in the (111) surface occupies 6.45 Å². Thus at 100% dispersion, the total surface area should be 666 m²/g-Ni.

and calcination and, optionally, reduction and passivation. The Ni loading, Ni surface area, and the code names of the HTC catalysts are shown in table 1.

2.2. XAFS measurement

X-ray absorption spectra of the catalysts at the Ni K-edge were measured in transmission mode at the Swiss Norwegian beam line (SNBL) at the European synchrotron radiation facility (ESRF) in Grenoble, France. The electron energy and the ring current were 6.0 GeV and 130–200 mA, respectively. The incident X-rays were monochromated by a Si(111) channel-cut monochromator and harmonics were rejected by a gold-coated mirror positioned with an angle of 7.0 mrad to the beam. The X-ray intensity was monitored by ion chambers and the estimated resolution was 1 eV at the Ni K-edge (8332 eV). The lengths of the ion chambers before and after the sample were 17 and 31 cm and the chambers were filled with pure nitrogen and an argon/nitrogen mixed gas (Ar/N₂ = 40/60), respectively. The data collection time for each data point in a scan was 1, 2, 3, and 4 s for the 7780–8280 (pre-edge), 8280–8380 (edge region), 8380–8710 (post-edge, $k = 3$–10 Å⁻¹), and 8710–9860 eV (post-edge $k = 10$–20 Å⁻¹) regions, respectively, and 3–5 scans were averaged. The energy difference between the post-edge data points was determined so that the difference in their k values was smaller than 0.05 Å⁻¹.

A sample was pressed into a self-supported wafer, mounted in an *in situ* cell, and cooled by liquid nitrogen to a measuring temperature of about 100 K. The samples in the oxidic and passivated state were measured under helium without further treatment. The samples in the reduced state were prepared by reduction of the oxidic samples in flowing hydrogen (60 ml/min) in the EXAFS cell. The samples were heated gradually (6 K/min) to 723 K and kept at 723 K for 30 min. The samples in the reduced state were measured under hydrogen.

2.3. XANES analysis

The spectra at the edge jump (8280–8400 eV) were simulated by a linear function of the references of the oxidic and reduced state to estimate the proportion of reduced Ni in the reduced and passivated state. The following formula was used:

$$(\text{XANES observed}) = f_1 \cdot (\text{XANES of oxidic state}) \\ + f_2 \cdot (\text{XANES of reduced state}), \quad (1)$$

where f_1 and f_2 are the fractions of the oxidic and reduced state, respectively. Both f_1 and f_2 were treated as free parameters in this analysis. The reference for the oxidic state was the oxidic sample and the reference for the reduced state the reduced HTC-400 sample for HTC-1.9, 4.5, 100, 200, and 400, and HTC-500 for the passivated HTC-500.

2.4. EXAFS analysis

The EXAFS data were analysed using the XDAP program [15,16]. The pre-edge background was approximated by a modified Victoreen curve and the background was subtracted using a cubic spline routine. The spectra were normalized by the edge jump. Standard deviations were calculated for each individual EXAFS data point as a measure of the random error in the final EXAFS function.

Reference spectra were calculated using FEFF7 [17,18] for several cluster models; Ni₈₅O₄₄ for oxidic Ni, Ni₂₀₁ for metallic Ni, and NiAl₁₃O₃₈ for Ni–Al contributions. The size of these clusters was determined so that the cluster size is big enough to simulate EXAFS spectra up to 7 Å. The multiple scattering effect was taken into account. As the number of free data points is limited, EXAFS functions of each path should be collected to decrease the number of parameters needed to analyse the observed data. The basic strategy is to regard all paths as ith shell contribution that include the scattering up to the ith shell. The reference EXAFS function of the ith shell was calculated as a sum of the EXAFS functions of such paths. Table 2 shows the shells of scatterers used to calculate reference spectra and the notation of the contributions. In the case of the reduced state, all references were made following this strategy. In the case of the oxidic state, the strategy was modified as follows. The spectra of the oxidic samples were fitted by the nearest Ni–O, nearest Ni–Ni, and the second nearest Ni–Ni contributions, while the second nearest Ni–O contribution was neglected because it is very weak. Scattering paths at the oxygen atoms surrounding the Ni cations were included to make reference spectra for the nearest and the second nearest Ni–Ni contributions. This approximation worked well down to small NiO clusters, because in our samples all the nickel cations are coordinated by six oxygen anions like in bulk NiO (see sections 3 and 4).

Table 2
Scattering paths used to calculate references.

References	Shells	Scatterers[a,b]
NiO	The first shell (Ni–O)	c, <u>o-1</u>
	The nearest Ni–Ni (Ni–Ni(o1))	c, o-1, <u>n-1</u>*
	The second nearest Ni–Ni (Ni–Ni(o2))	c, o-1, n-1, o-2, <u>n-2</u>*
Ni metal	The first shell (Ni–Ni(m1))	c, <u>n-1</u>
	The second shell (Ni–Ni(m2))	c, n-1, <u>n-2</u>
	The third shell (Ni–Ni(m3))	c, n-1, n-2, <u>n-3</u>
	The fourth shell (Ni–Ni(m4))	c, n-1, n-2, n-3, <u>n-4</u>
	The fifth shell (Ni–Ni(m5))	c, n-1, n-2, n-3, n-4, <u>n-5</u>

[a] The underlined shell is always contained to make a reference.
[b] Denotations of the scatterers: c, the central Ni atom; n-i, ith nearest Ni atoms; n-i*, ith nearest Ni atoms and coordinating O atoms to the Ni atoms; o-i, ith nearest O atoms.

The coefficient that describes the multi-body effects (S_0^2) was determined by requiring that the coordination numbers of the first shells obtained from the experimental EXAFS spectra of Ni foil and NiO are equal to 12 and 6, respectively. S_0^2 of the reduced and oxidic state were 0.87 and 1.03, respectively, which agrees with reported values [7]. The S_0^2 coefficient of the Ni–Al contribution was assumed to be equal to that of NiO.

The k^3-weighted EXAFS functions were Fourier transformed and fitted in R space. Free parameters were interatomic distance, coordination number, Debye–Waller factor and the correction of the edge energy. The errors of the parameters were statistically estimated using the random errors of the observed data. The fitting R ranges for the oxidic and passivated samples were 1.0–4.1 and 1.0–3.0 Å, respectively. The spectra of the oxidic samples were fitted by Ni–O, Ni–Ni(o1) and Ni–Ni(o2) (or Ni–Al(2)) contributions, and Ni–O, Ni–Ni(o1), and Ni–Ni(m1) contributions were used to fit the spectra of the passivated samples. The contribution of the third shell (the second nearest Ni–O) of NiO was not taken into account because the amplitude of the contribution was negligible. In the case of the reduced state, the Fourier-transformed spectra were divided into two parts. The peaks at 1.0–2.7 Å were fitted by first shell Ni–Ni(m1) and Ni–O contributions and those at 2.7–5.5 Å by higher shell Ni–Ni(m2), Ni–Ni(m3), Ni–Ni(m4), and Ni–Ni(m5) contributions. The multiple scattering effect of the first shell was subtracted from the observed spectra to fit the higher shell contributions. ΔE_0's of the higher shell contributions were fixed at the ΔE_0 of the Ni–Ni(m1) contribution to reduce the number of parameters.

3. Results

3.1. Oxidic state

Figure 1 shows the k^3-weighted EXAFS functions ($k^3 \cdot \chi(k)$) of the HTC-1.9 and HTC-500 samples in the oxidic state. In each spectrum, the S/N ratio is excellent up to 17 Å^{-1}. Figure 2 shows the corresponding Fourier-transformed EXAFS functions ($k^3 \cdot \chi(k)$) together with their curve fittings. The Fourier-transformed k range and fitted R range were 3–17 and 1.0–4.1 Å, respectively. The Fourier-transformed spectra were fitted by three shells; the EXAFS of NiO, HTC-100, HTC-200, HTC-400, and HTC-500 were fitted with Ni–O, Ni–Ni(o1), and Ni–Ni(o2) contributions. The Ni–Al(2) contribution was employed instead of the Ni–Ni(o2) contribution to fit the spectra of HTC-1.9 and HTC-4.5, since the small peak at 3.0–4.1 Å in the spectra of HTC-1.9 and HTC-4.5 could not be fitted by a Ni–Ni contribution. The F test [19] of the fit of these spectra implied that the goodness of the fit was significantly better with the addition of the Ni–Al(2) contribution than the Ni–Ni(o2) contribution. The first and second shells of all observed spectra were reproduced well by the calculated spectra. The intensity of the second ($R = 2.2$–3.0 Å) and third peak (3.1–4.2 Å) decreased with decreasing loading, while the intensity of the first peak remained unchanged. FEFF simulation showed that the first, second, and third peaks were primarily due to the Ni–O, nearest Ni–Ni and second nearest Ni–Ni contributions, respectively. The contribution of the second nearest Ni–O was more than twenty times weaker than the other contributions and a clear peak was not observed in a Fourier-transformed k^3-weighted EXAFS function.

Table 3 shows the structural parameters in the oxidic state determined by EXAFS analysis. The coordination number of the Ni–O contribution was always 6 regardless of loading, equal to that of bulk NiO. The $\Delta\sigma^2$ values of the NiO were larger than that of bulk NiO by 2.0–3.3 × 10^{-3} Å^2, and did not depend very much on the loading. The Ni–O distances of the samples were shorter than that of bulk NiO and became shorter with decreasing loading. The Ni–O distance of bulk NiO was 2.08 Å, and that of HTC-500 and HTC-1.9 was 2.06 and 2.04 Å, respectively.

The CN's of the second shell (the nearest Ni–Ni contribution) of the oxidic samples were much smaller than that of bulk NiO and decreased with decreasing loading from 6.6 in HTC-500 to 3.1 in HTC-1.9. The nearest Ni–Ni distance was almost the same as that of bulk NiO. The corresponding Debye–Waller factors were larger than that in bulk NiO and increased with decreasing loading. In
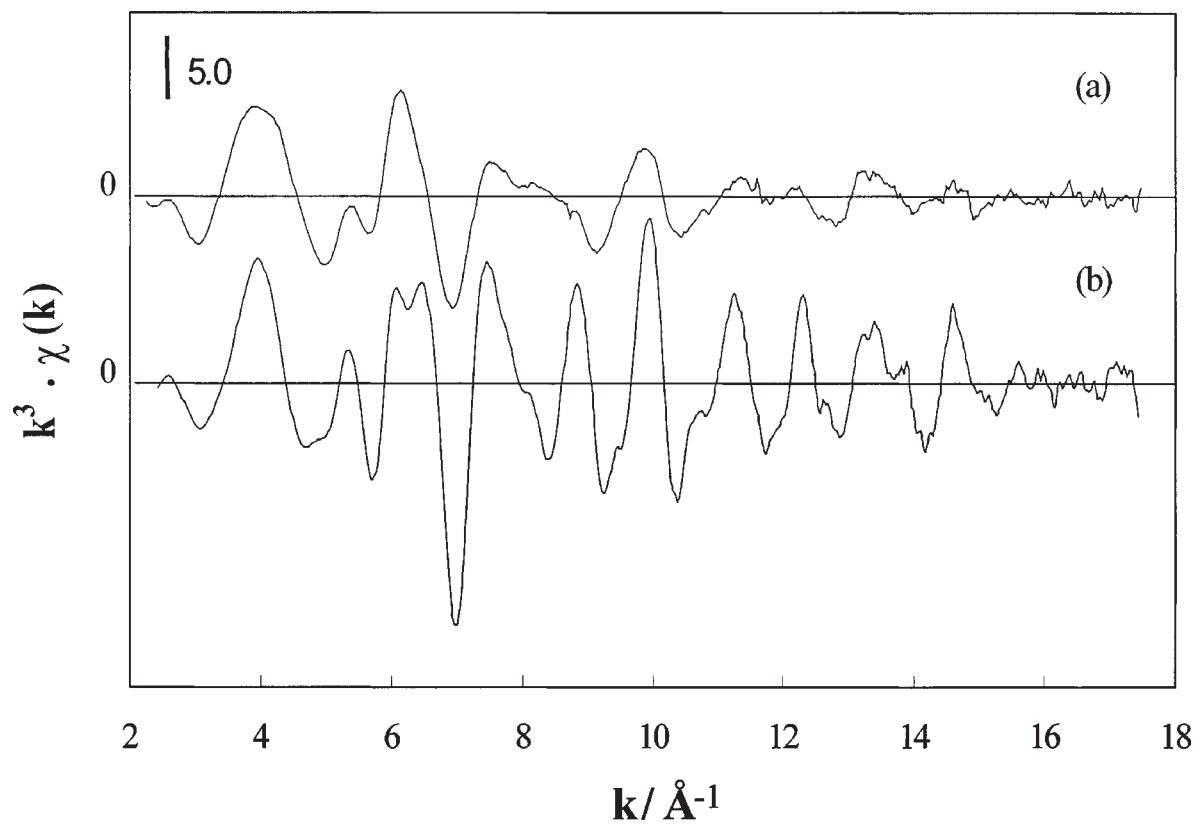
Figure 1. k^3-weighted EXAFS functions ($k^3 \cdot \chi(k)$) of HTC-1.9 (a) and HTC-500 (b) in the oxidic state.
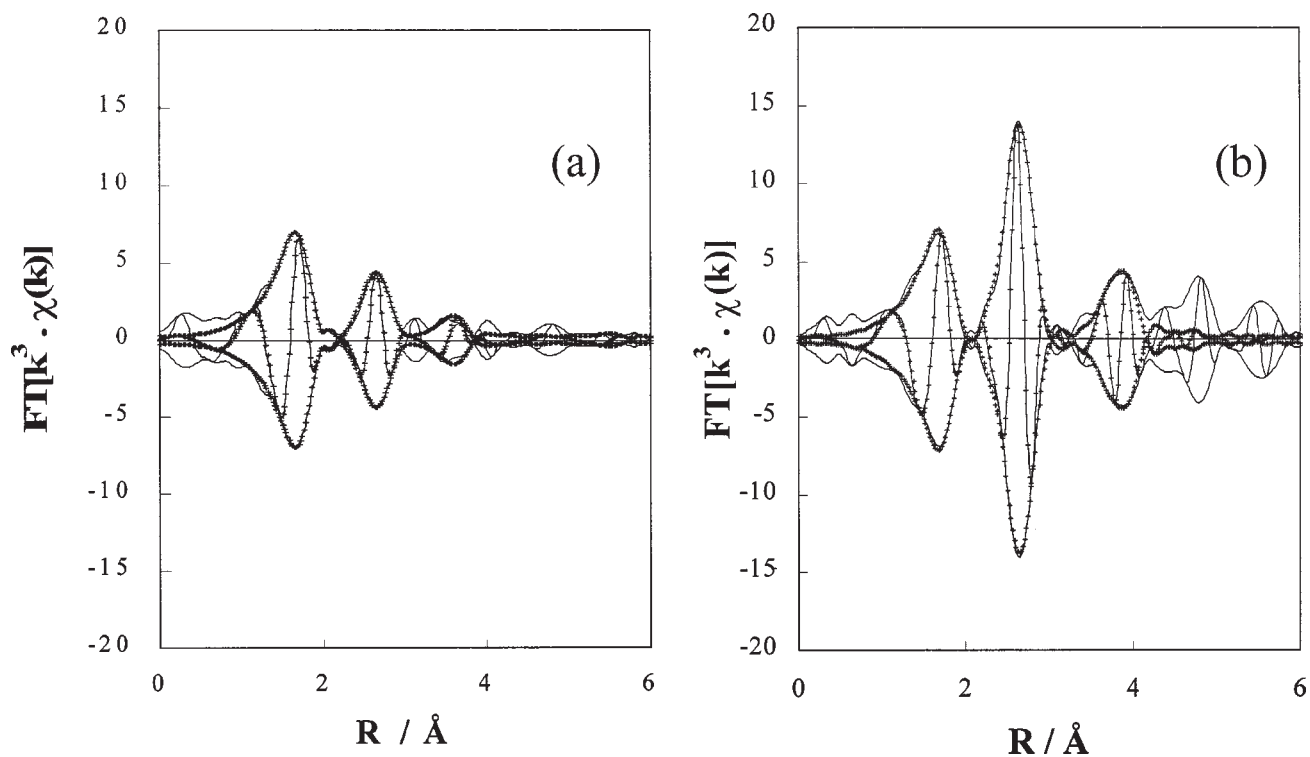

Figure 2. Fourier transformed k^3-weighted EXAFS functions ($k^3 \cdot \chi(k)$) of HTC-1.9 (a) and HTC-500 (b) in the oxidic state (solid lines) with their curve fitting results (dotted lines). Absolute values as well as imaginary parts are displayed.

Table 3
Structural parameters of HTC(ox) catalysts derived from the EXAFS analysis.

Sample	Shells	CN(CN*)[a]	Distance (Å)[a]	$\Delta\sigma^2$ (10^{-3}Å^2)	ΔE_0 (eV)
NiO	Ni–O	6.0 ± 0.3 (6.0)	2.08 ± 0.01 (2.09)	−0.3 ± 1.1	−3.3 ± 0.4
	Ni–Ni(o1)	11.8 ± 0.5 (12.0)	2.94 ± 0.01 (2.95)	1.7 ± 0.5	−0.5 ± 0.4
	Ni–Ni(o2)	5.3 ± 0.6 (6.0)	4.16 ± 0.01 (4.18)	1.7 ± 1.0	−3.2 ± 0.7
HTC-500(ox)	Ni–O	6.0 ± 0.3	2.06 ± 0.01	2.4 ± 1.4	−1.9 ± 0.5
	Ni–Ni(o1)	6.6 ± 0.7	2.96 ± 0.01	3.4 ± 1.2	−0.3 ± 0.9
	Ni–Ni(o2)	1.7 ± 0.6	4.18 ± 0.03	1.7 ± 3.2	−2.4 ± 2.3
HTC-400(ox)	Ni–O	6.0 ± 0.4	2.05 ± 0.01	2.6 ± 1.5	−1.2 ± 0.5
	Ni–Ni(o1)	5.2 ± 0.7	2.96 ± 0.01	3.2 ± 1.5	0.1 ± 1.1
	Ni–Ni(o2)	1.4 ± 0.7	4.18 ± 0.04	2.8 ± 4.7	−3.0 ± 3.0
HTC-200(ox)	Ni–O	5.9 ± 0.3	2.05 ± 0.01	1.6 ± 1.3	−0.6 ± 0.5
	Ni–Ni(o1)	4.0 ± 0.7	2.98 ± 0.02	3.6 ± 2.1	−0.6 ± 1.5
	Ni–Ni(o2)	0.9 ± 0.7	4.16 ± 0.06	2.5 ± 7.3	1.6 ± 4.9
HTC-100(ox)	Ni–O	6.3 ± 0.3	2.04 ± 0.01	2.7 ± 1.4	−0.2 ± 0.5
	Ni–Ni(o1)	3.7 ± 0.8	3.00 ± 0.02	4.7 ± 2.6	−1.1 ± 1.8
	Ni–Ni(o2)	0.7 ± 0.7	4.17 ± 0.07	2.1 ± 9.2	1.3 ± 6.3
HTC-4.5(ox)	Ni–O	5.9 ± 0.4	2.04 ± 0.01	2.7 ± 1.6	−0.6 ± 0.7
	Ni–Ni(o1)	3.9 ± 1.1	2.98 ± 0.03	6.5 ± 3.6	0.1 ± 3.1
	Ni–Ni(o2)	–	–	–	–
	Ni–Al(2)	1.2 ± 0.7	4.02 ± 0.07	2.3 ± 9.1	4.0 ± 4.8
HTC-1.9(ox)	Ni–O	6.3 ± 0.5	2.04 ± 0.01	2.9 ± 1.6	−0.6 ± 0.6
	Ni–Ni(o1)	3.1 ± 1.3	2.98 ± 0.04	6.1 ± 4.7	3.2 ± 4.9
	Ni–Ni(o2)	–	–	–	–
	Ni–Al(2)	3.4 ± 1.7	3.96 ± 0.07	11.0 ± 9.8	9.7 ± 3.7

[a] Values in parentheses are coordination numbers and distances derived from XRD [22].

the low loading samples, the difference in $\Delta\sigma^2$ of the Ni–Ni contribution between particle and bulk NiO is larger than that of the $\Delta\sigma^2$ of the Ni–O contribution. The CN's of the second nearest Ni–Ni were also smaller than that of bulk NiO. They decreased with decreasing loading and disappeared below 4.5 wt% Ni loading. The distance of the second nearest Ni–Ni is almost the same as that of bulk NiO and was not affected by loading. The $\Delta\sigma^2$ were slightly larger than that of bulk NiO, but did not vary much.

A Ni–Al contribution was observed at 3.96–4.02 Å at and below 4.5 wt% Ni loading. The "nearest" Ni–Al contribution (Ni(0, 0, 0)–Al(a/2, a/2, 0)) was not observed and only the second nearest contribution (Ni(0, 0, 0)–Al(a, 0, 0)) was observed. The distance of the Ni–Al contribution was shorter than the second nearest Ni–Ni by 0.17 Å.

3.2. Reduced state

Figure 3 shows the k^3-weighted EXAFS functions of the HTC-1.9 and HTC-500 samples in the reduced state. The S/N ratio is good up to 17 Å^{-1}. Figure 4 shows the corresponding FT's (k range of 3–17 Å^{-1}) and curve fittings. The $R = 1.0$–2.7 Å range was fitted by the nearest metal Ni–Ni and Ni–O (for HTC-1.9, HTC-4.5, and HTC-100) contributions and the $R = 2.7$–5.5 Å range was fitted by the 2nd–5th metal Ni–Ni shells. The effect of multiple scattering of the nearest Ni–Ni and Ni–O contributions was subtracted from the contributions in the 2.7–5.5 Å range.

As shown in figure 4, the observed spectra were reproduced well by the calculated spectra.

Table 4 shows the results of the curve fittings. The Ni–Ni distances of the 1st–5th shells were similar to those of the Ni foil, and were insensitive to the loading. The Debye–Waller factors of the 1st–5th shells were larger than those of the Ni foil and increased slightly as loading decreased.

Ni–O contributions were observed for the HTC-1.9, HTC-4.5 and HTC-100 samples. To estimate the particle size from the CN of the Ni–Ni contribution, the proportion of reduced Ni should be determined accurately. The CN of the Ni–O contribution is not accurate enough because the corresponding FT peak is overlapped by the nearest Ni–Ni contributions. Therefore, the proportion of reduced Ni was determined from the XANES of the reduced samples by fitting with a linear function of the references of the oxidic and reduced state. Figure 5 shows the XANES of the HTC-1.9, HTC-4.5, HTC-100, and HTC-200 samples together with the fitting results, and table 5 shows the fractions of the reduced and oxidic states and the proportion of reduced nickel. The observed XANES was reproduced perfectly by a simple sum of the oxidised and reduced references. The proportion of reduced nickel estimated from XANES agreed with that from the EXAFS data within the error of the coordination numbers. However, the accuracy of the proportion obtained from XANES is much better than that from EXAFS. The corrected CN's taking the proportion of reduced nickel into account (CN of the metal particles) are shown in square brackets in table 4. The k^1-weighted EXAFS
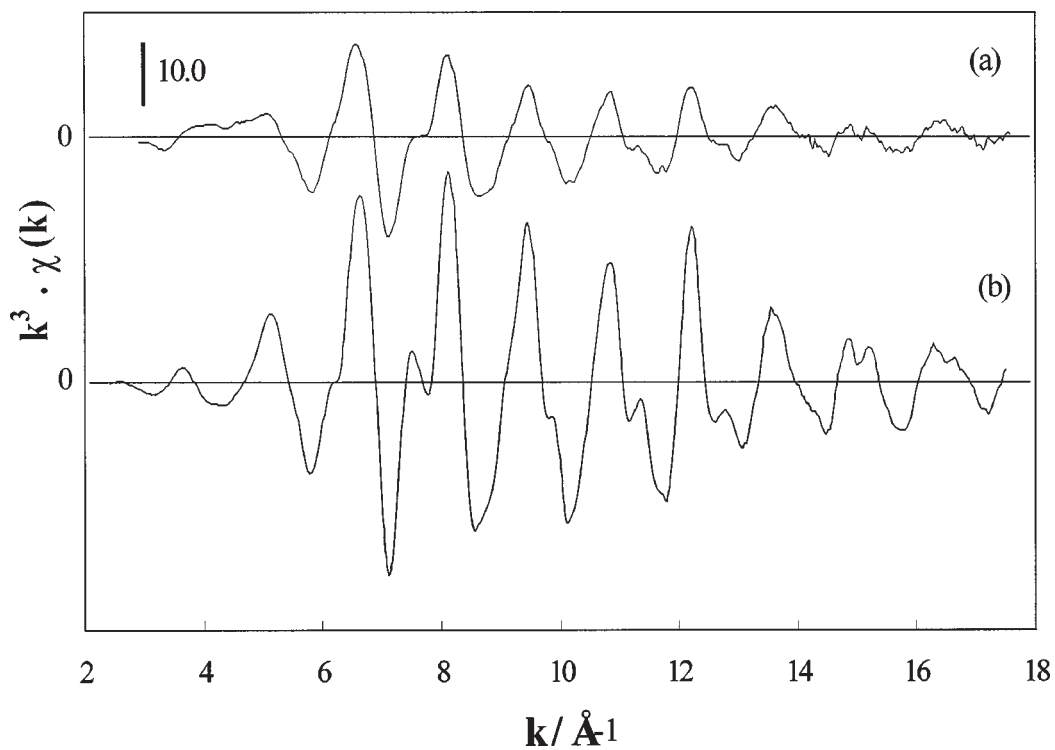
Figure 3. k^3-weighted EXAFS functions ($k^3 \cdot \chi(k)$) of HTC-1.9 (a) and HTC-500 (b) in the reduced state.
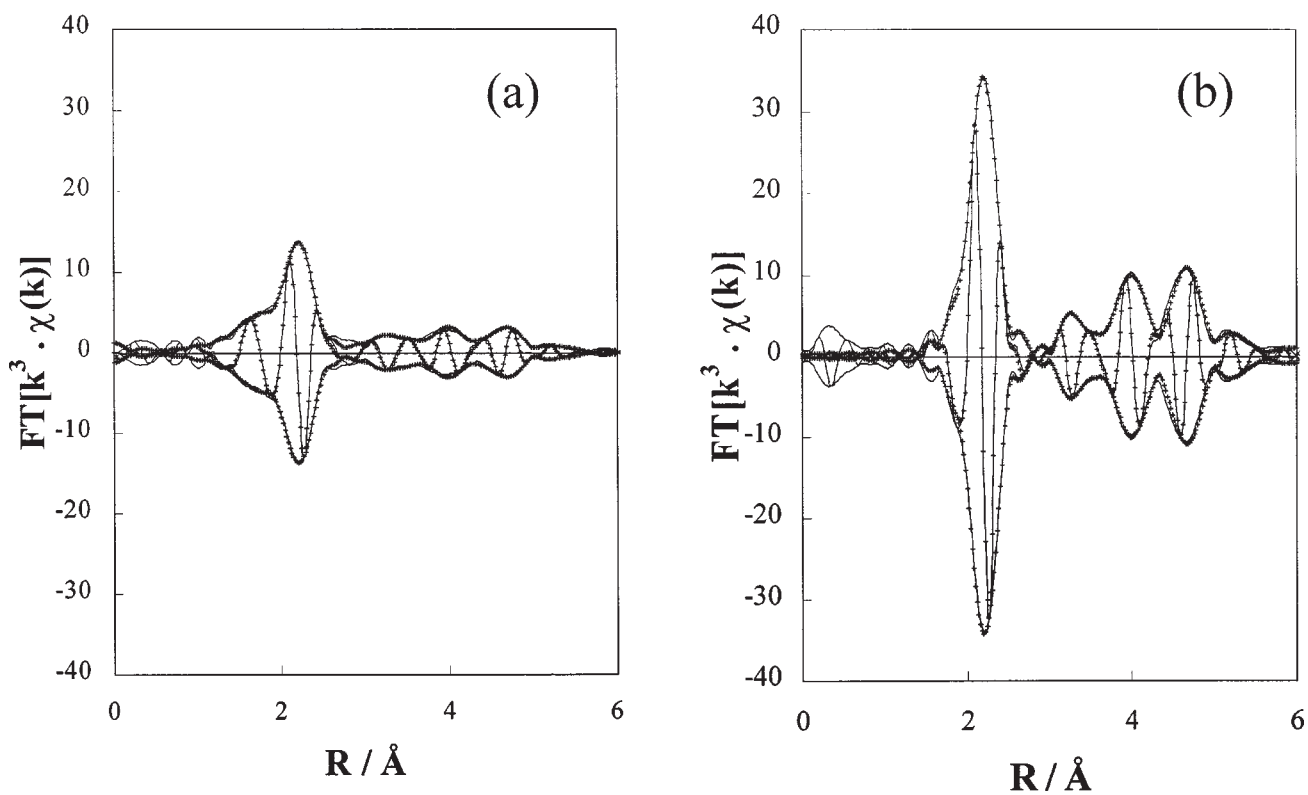
Figure 4. Fourier transformed k^3-weighted EXAFS functions ($k^3 \cdot \chi(k)$) of HTC-1.9 (a) and HTC-500 (b) in the reduced state (solid lines) with their curve fitting results (dotted lines). Absolute values as well as imaginary parts are displayed.

Table 4
Structural parameters of the reduced Ni/θ-Al$_2$O$_3$ catalysts derived by EXAFS analysis.

Sample	Shell	CN[a,b]	Distance (Å)[a]	$\Delta\sigma^2$ (10^{-3}Å^2)	ΔE_0 (eV)
Ni foil	Ni–Ni(m1)	12.0 ± 0.3 (12.0)	2.48 ± 0.01 (2.49)	0.8 ± 0.3	−6.8 ± 0.2
	Ni–Ni(m2)	5.4 ± 1.2 (6.0)	3.56 ± 0.01 (3.52)	1.4 ± 2.2	−6.8
	Ni–Ni(m3)	24.5 ± 2.5 (24.0)	4.30 ± 0.01 (4.32)	2.3 ± 1.0	−6.8
	Ni–Ni(m4)	12.4 ± 2.0 (12.0)	4.97 ± 0.01 (4.98)	2.2 ± 1.4	−6.8
	Ni–Ni(m5)	16.1 ± 5.2 (24.0)	5.57 ± 0.02 (5.57)	1.1 ± 3.1	−6.8
HTC-500(r)	Ni–Ni(m1)	9.5 ± 0.4	2.48 ± 0.01	1.1 ± 0.4	−6.7 ± 0.3
	Ni–Ni(m2)	3.6 ± 1.2	3.51 ± 0.01	1.8 ± 3.5	−6.7
	Ni–Ni(m3)	14.6 ± 2.5	4.30 ± 0.01	2.2 ± 1.7	−6.7
	Ni–Ni(m4)	6.7 ± 2.1	4.97 ± 0.01	2.3 ± 2.6	−6.7
	Ni–Ni(m5)	8.8 ± 5.8	5.58 ± 0.03	1.7 ± 6.5	−6.7
HTC-400(r)	Ni–Ni(m1)	8.8 ± 0.4	2.48 ± 0.01	1.7 ± 0.5	−6.7 ± 0.3
	Ni–Ni(m2)	3.6 ± 1.4	3.51 ± 0.01	3.7 ± 4.4	−6.7
	Ni–Ni(m3)	12.3 ± 2.6	4.30 ± 0.01	2.7 ± 2.2	−6.7
	Ni–Ni(m4)	5.5 ± 2.3	4.97 ± 0.01	3.1 ± 3.6	−6.7
	Ni–Ni(m5)	7.1 ± 5.7	5.59 ± 0.04	2.0 ± 8.2	−6.7
HTC-200(r)	Ni–Ni(m1)	8.7 ± 0.4	2.48 ± 0.01	1.8 ± 0.5	−6.2 ± 0.3
	Ni–Ni(m2)	3.5 ± 1.4	3.50 ± 0.01	3.5 ± 4.5	−6.2
	Ni–Ni(m3)	11.5 ± 2.5	4.30 ± 0.01	2.4 ± 2.2	−6.2
	Ni–Ni(m4)	5.0 ± 2.2	4.96 ± 0.01	2.7 ± 3.7	−6.2
	Ni–Ni(m5)	8.0 ± 6.2	5.59 ± 0.04	2.3 ± 7.8	−6.2
HTC-100(r)	Ni–O	1.3 ± 0.3	2.02 ± 0.04	2.2 ± 6.8	−9.1 ± 1.7
	Ni–Ni(m1)	7.8 ± 0.7 [8.6 ± 0.7]	2.48 ± 0.01	2.0 ± 0.8	−6.7 ± 1.0
	Ni–Ni(m2)	3.9 ± 1.6 [4.3 ± 1.7]	3.51 ± 0.02	5.1 ± 4.7	−6.7
	Ni–Ni(m3)	10.7 ± 2.7 [11.7 ± 3.0]	4.30 ± 0.01	3.2 ± 2.7	−6.7
	Ni–Ni(m4)	4.3 ± 2.4 [4.8 ± 2.6]	4.97 ± 0.02	3.2 ± 4.8	−6.7
	Ni–Ni(m5)	7.1 ± 5.8 [7.8 ± 6.4]	5.60 ± 0.05	2.8 ± 9.1	−6.7
HTC-4.5(r)	Ni–O	1.4 ± 0.3	2.01 ± 0.03	0.2 ± 4.9	−7.9 ± 1.5
	Ni–Ni(m1)	6.8 ± 0.7 [8.5 ± 0.8]	2.47 ± 0.01	2.3 ± 1.0	−5.8 ± 1.1
	Ni–Ni(m2)	2.8 ± 1.5 [3.5 ± 1.9]	3.49 ± 0.02	3.7 ± 5.7	−5.8
	Ni–Ni(m3)	7.5 ± 2.6 [9.4 ± 3.3]	4.30 ± 0.02	2.7 ± 3.5	−5.8
	Ni–Ni(m4)	2.5 ± 2.1 [3.2 ± 2.6]	4.96 ± 0.02	2.0 ± 6.6	−5.8
	Ni–Ni(m5)	10.8 ± 8.5 [13.4 ± 10.6]	5.60 ± 0.04	7.2 ± 9.2	−5.8
HTC-1.9(r)	Ni–O	2.9 ± 0.4	2.00 ± 0.02	2.9 ± 3.6	−7.2 ± 1.0
	Ni–Ni(m1)	5.3 ± 0.7 [8.1 ± 1.1]	2.47 ± 0.01	2.8 ± 1.4	−5.5 ± 1.5
	Ni–Ni(m2)	5.4 ± 2.3 [8.2 ± 3.6]	3.48 ± 0.02	11.1 ± 5.9	−5.5
	Ni–Ni(m3)	5.1 ± 2.8 [7.7 ± 4.2]	4.29 ± 0.02	3.2 ± 5.6	−5.5
	Ni–Ni(m4)	1.5 ± 2.2 [2.2 ± 3.4]	4.95 ± 0.04	1.9 ± 11.8	−5.5
	Ni–Ni(m5)	12.4 ± 11.0 [18.7 ± 16.7]	5.59 ± 0.04	13.3 ± 9.9	−5.5

[a] Values in parentheses "( )" are coordination numbers and distances derived by XRD [23].
[b] Values in square brackets "[ ]" are the CN for the metal particles taking the proportion of reduced Ni into account (CN of metal particles).

function of HTC-400 in the reduced state was analysed to determine if the sample was completely reduced, because a Ni–O contribution is enhanced with k^1 rather than k^3 weighting. The Ni–O contribution was not observed in a k^1-weighted EXAFS function of HTC-400 in the reduced state either, which means that almost all the nickel in the sample was reduced and only a small amount (<10%) may have remained unreduced.

The CN's of the first and fifth shell decreased as the loading decreased. The accuracy of the CN of the first shell is quite good, but that of the 2nd–5th shells contains a large error. Especially, the errors in the CN's of the second and fifth shells were huge and these CN's were therefore not used to estimate the particle size. The distances and Debye–Waller factors of the Ni–Ni contributions of the reduced samples were close to those of Ni foil. On the other hand,

the distance of the Ni–O contribution (2.00–2.02 Å) was shorter than that in the oxidic state.

3.3. Passivated state

Table 6 shows the results of the XANES fitting of the samples in the passivated state. The residuals were less than 2% and the sums of the fractions of the reduced and oxidic state ($f_1 + f_2$) were close to unity. The results show that the proportion of the reduced nickel was 10–27% and increased with loading.

Figure 6 shows the Fourier-transformed EXAFS functions ($k^3 \cdot \chi(k)$) of HTC-100 and HTC-500 in the passivated state together with their curve fittings. The R range of 1.0–3.0 Å was fitted by three shells: Ni–O, the nearest Ni–Ni of nickel oxide (Ni–Ni(o1)) and the nearest Ni–Ni
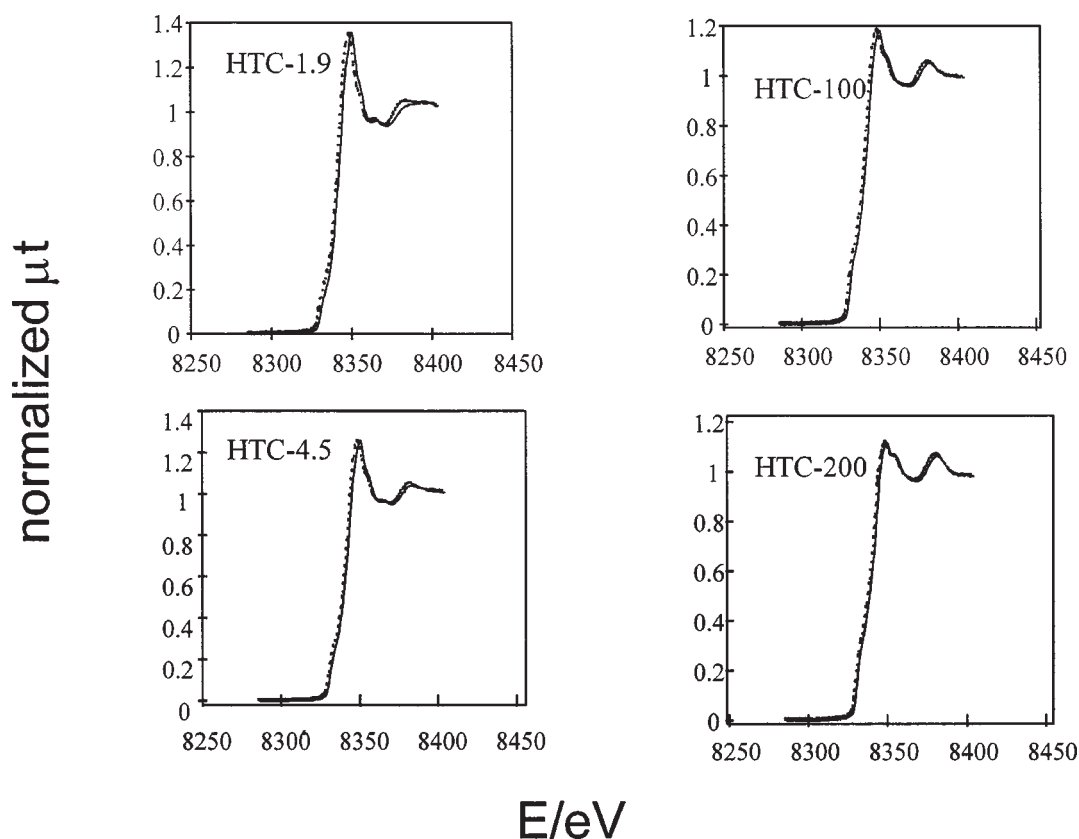
Figure 5. XANES spectra of HTC-1.9, 4.5, 100, and 200 in the reduced state with their curve fitting results.

Table 5
Results of the XANES analysis of the reduced Ni/θ-Al$_2$O$_3$ catalysts.

Sample	f_1[a]	f_2[b]	Proportion of reduced Ni (%)	$f_1 + f_2$
HTC-1.9(r)	0.341 ± 0.007	0.661 ± 0.007	66	1.002
HTC-4.5(r)	0.205 ± 0.004	0.797 ± 0.004	80	1.002
HTC-100(r)	0.093 ± 0.003	0.907 ± 0.003	91	1.000
HTC-200(r)	0.003 ± 0.002	0.999 ± 0.002	100	1.002

[a] Fraction of oxidic state, see formula (1).
[b] Fraction of reduced state, see formula (1).

Table 6
Results of the XANES analysis of the passivated Ni/θ-Al$_2$O$_3$ catalysts.

Sample	f_1[a]	f_2[b]	Proportion of reduced Ni (%)	$f_1 + f_2$
HTC-100(p)	0.857 ± 0.008	0.136 ± 0.009	14	0.993
HTC-200(p)	0.896 ± 0.005	0.100 ± 0.005	10	0.996
HTC-400(p)	0.811 ± 0.004	0.188 ± 0.004	19	0.999
HTC-500(p)	0.726 ± 0.010	0.273 ± 0.009	27	0.999

[a] Coefficient of oxidic state, see formula (1).
[b] Coefficient of reduced state, see formula (1).

of the nickel metal (Ni–Ni(m1)). In the spectrum of HTC-100(p), Ni–O and Ni–Ni(o1) contributions dominated and only a small contribution of metallic Ni–Ni was observed. Table 7 shows the structural parameters derived by curve fitting of the EXAFS spectra. As the three shells overlapped heavily as shown in figure 6, the errors of the structural parameters were larger than those obtained for the oxidic and reduced states. The values in square brackets in table 7

are the corrected CN's for nickel metal particles; they are about 6–7. The error in the corrected CN is substantial because the contribution of metallic Ni–Ni and the proportion of metallic Ni are small. The distances and Debye–Waller factors of the Ni–O, Ni–Ni(o1), and Ni–Ni(m1) contributions agreed with those of the oxidic and reduced state. The Ni–O distance was slightly shorter and Ni–O and Ni–Ni(o1) Debye–Waller factors were larger than for bulk NiO.
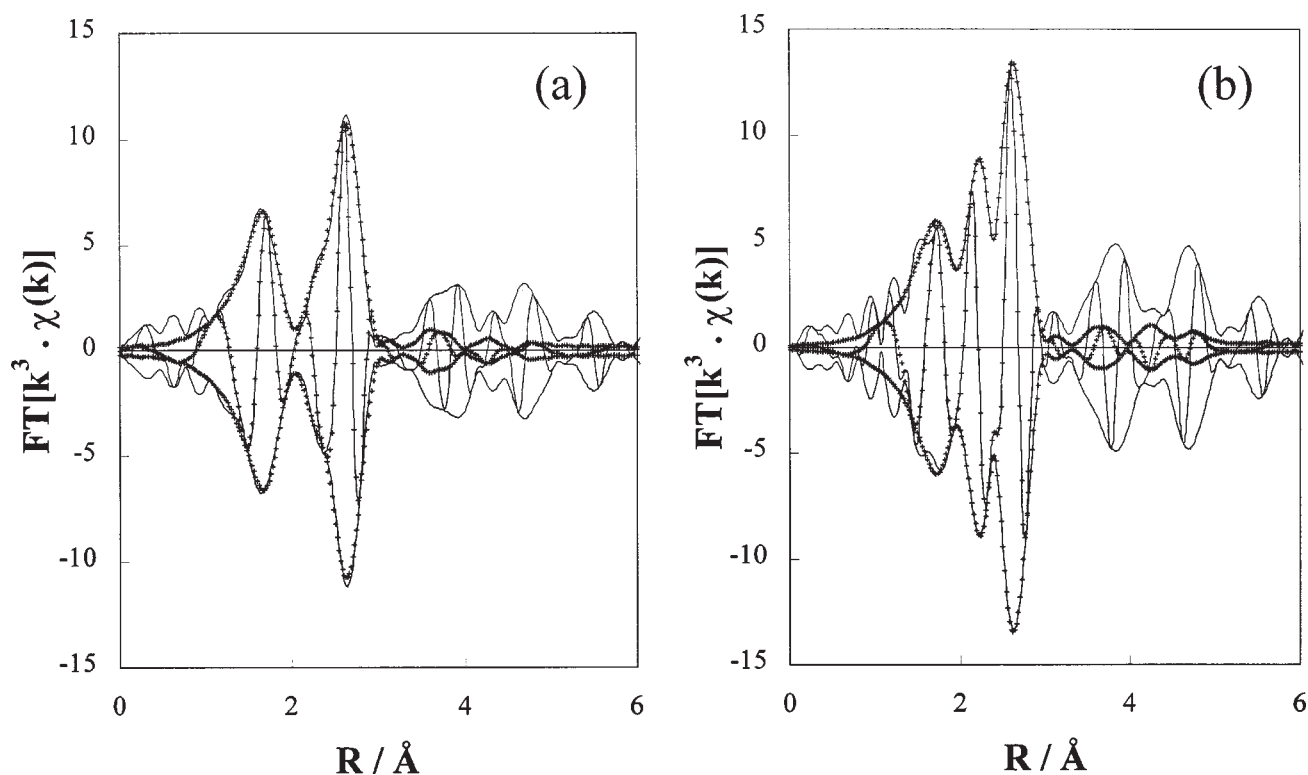
Figure 6. Fourier-transformed k^3-weighted EXAFS functions ($k^3 \cdot \chi(k)$) of HTC-100 (a) and HTC-500 (b) in the passivated state (solid lines) with their curve fitting results (dotted lines). Absolute values as well as imaginary parts are displayed.

Table 7
Structural parameters of the passivated Ni/θ-Al$_2$O$_3$ catalysts derived by EXAFS analysis.

Sample	Shell	CN[a]	Distance (Å)	$\Delta\sigma^2$ (10^{-3}Å^2)	ΔE_0 (eV)
HTC-500(p)	Ni–O	4.8 ± 0.4	2.07 ± 0.01	2.5 ± 2.3	−2.9 ± 0.7
	Ni–Ni(m1)	2.0 ± 0.8 [7.3 ± 2.9]	2.49 ± 0.03	0.7 ± 3.3	−1.7 ± 4.5
	Ni–Ni(o1)	5.9 ± 0.7	2.95 ± 0.01	3.2 ± 1.5	0.5 ± 1.3
HTC-400(p)	Ni–O	6.0 ± 0.5	2.06 ± 0.01	4.5 ± 2.2	−1.7 ± 0.7
	Ni–Ni(m1)	1.1 ± 0.9 [5.9 ± 4.8]	2.49 ± 0.05	1.0 ± 6.1	−2.0 ± 8.3
	Ni–Ni(o1)	6.0 ± 0.7	2.95 ± 0.01	3.9 ± 1.7	0.4 ± 1.3
HTC-200(p)	Ni–O	6.2 ± 0.3	2.05 ± 0.01	3.1 ± 1.5	−0.7 ± 0.5
	Ni–Ni(m1)	0.7 ± 0.9 [7.0 ± 9.0]	2.50 ± 0.04	4.0 ± 5.1	−1.0 ± 7.9
	Ni–Ni(o1)	5.9 ± 0.4	2.96 ± 0.01	4.1 ± 1.7	−0.7 ± 1.3
HTC-100(p)	Ni–O	5.7 ± 0.3	2.05 ± 0.01	2.7 ± 1.6	−1.2 ± 0.6
	Ni–Ni(m1)	0.8 ± 0.9 [5.8 ± 6.6]	2.51 ± 0.04	4.0 ± 6.8	−1.0 ± 7.4
	Ni–Ni(o1)	5.6 ± 0.4	2.96 ± 0.01	4.1 ± 1.8	−0.6 ± 1.4

[a] Values in square brackets "[ ]" are the CN for the metal particles taking the proportion of reduced Ni into account (CN of metal particles).

4. Discussion

4.1. Oxidic state

The results of the HTC catalyst in the oxidic state clearly showed that the Ni cations in the oxide particles are surrounded by six oxygen anions as in bulk NiO. A significant difference appeared in the CN's of the Ni–Ni contributions, they decreased dramatically with decreasing loading. Especially, the Ni–Ni(o2) CN decreased to zero in the spectra of HTC-1.9 and HTC-4.5. The small Ni–Ni coordination numbers suggest that the NiO particles on the Al$_2$O$_3$ sup- port are small. Table 8 shows the CN's of the nearest and the second nearest Ni–Ni contributions of various hypothetical NiO particles. The Ni–Ni CN's are affected by the shape and size of the NiO particles. Especially, in the case of a Ni monolayer in the NiO(111) orientation, the CN of the second nearest Ni–Ni is always zero regardless of the particle size. Comparison of tables 3 and 7 suggests that the NiO particles in the oxidic catalysts were small and were predominantly built up of successive (111) layers. The observed CN's did not agree with those of cubic NiO (100) particles (model 9) and with a one layer NiO(100) model (models 13–15). Even in the smallest cu-

Table 8
CN(Ni–Ni(o1)) and CN(Ni–Ni(o2)) in various small NiO particles.

No. of model	Structure[a]	O/Ni ratio	CN(Ni–Ni(o1))	CN(Ni–Ni(o2))	Corresponding sample
1	Ni_4(111) 1 layer	16/4	2.5	0.0	HTC-1.9
2	Ni_7(111) 1 layer	24/7	3.4	0.0	HTC-4.5
3	$Ni_7 + Ni_1$(111) 2 layer	26/8	3.8	0.5	HTC-100
4	$Ni_7 + Ni_3$(111) 2 layer	31/10	4.8	1.2	HTC-200
5	$Ni_7 + Ni_6$(111) 2 layer	33/13	5.5	1.4	HTC-400
6	Ni_7(111) + Ni_{13}(100) cubic		6.0	2.1	
7	$Ni_7 + Ni_6 + Ni_3$(111) 3 layer	41/16	6.0	1.4	HTC-500
8	$Ni_7 + Ni_{12}$(111) 2 layer	49/19	6.0	1.6	HTC-500
9	Ni_{13}(100) cubic ($Ni_4 + Ni_5 + Ni_4$)		5.5	1.9	
10	$Ni_7 + Ni_{12} + Ni_3$(111) 3 layer (1)	61/22	6.7	2.4	HTC-500
11	$Ni_7 + Ni_{12} + Ni_3$(111) 3 layer (2)	57/22	6.0	1.9	HTC-500
12	$Ni_7 + Ni_{30}$(111) 2 layer		5.6	1.1	
13	Ni_5(100) 1 layer		1.6	1.6	
14	Ni_9(100) 1 layer		2.7	1.8	
15	Ni_{13}(100) 1 layer		2.5	2.5	

[a] Oxygen atoms are omitted. The (111) layers of Ni cations are considered to be sandwiched by two O layers.

bic model (model 9), the CN of the second nearest Ni–Ni contribution was larger than that of the HTC catalysts. In the case of a one layer (100) model, the CN's of the second nearest Ni–Ni were similar to the CN of the nearest Ni–Ni contributions, which does not agree with the observed coordination numbers.

The CN's of the Ni–Ni contributions of the HTC-1.9, HTC-4.5, HTC-100, HTC-200, and HTC-400 samples were similar to those of models 1, 2, 3, 4, and 5, respectively. In the case of HTC-500, several structures are possible (models 7, 8, 10, and 11). However, each of these structures consists predominantly of (111) planes like the low loading samples. The differences between the observed coordination numbers and those of the models may come from the heterogeneity of the small NiO particles. For example, the NiO particles in HTC-1.9(ox) may be a mixture of Ni_4O_x and Ni_7O_x particles. We conclude that the quantitative analysis of the CN's of the Ni–Ni contributions clearly shows that the NiO particles in the HTC catalysts are small NiO particles with predominant (111) planes.

Figure 7 shows the NiO particle size as a function of loading. Below 12 wt%, the particle size was almost constant and was smaller than $Ni_{10}O_x$. The particle size began to increase above 12 wt% and was then more or less proportional to the loading. The data suggest that small Ni particles of a limited size ($Ni_{7-10}O_x$) are formed at low loading. At ca. 12 wt% Ni loading, all nucleation sites on the support surface are covered with such particles and with increasing Ni loading the NiO particles grow further. The density of the NiO particles above 7 wt% is estimated to be 0.5 nm^{-2} from the inclination of the dotted line in figure 7.

The shape of the NiO particles suggests that the particles interact strongly with the alumina support, because bulk NiO has the NaCl structure and NaCl crystals usually are not cleaved along the (111) plane. In addition, a Ni–Al contribution was observed at low loading, which also suggests that the particles interact strongly with the Al₂O₃ support. To accommodate NiO particles with pre-
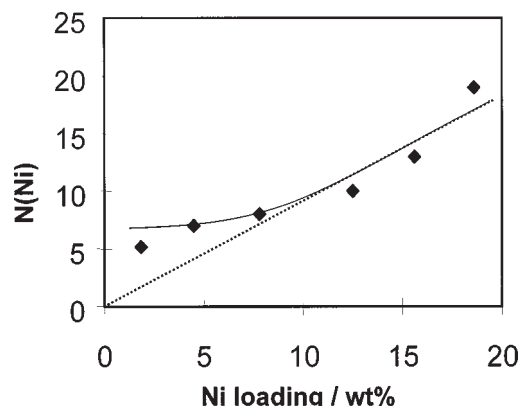

Figure 7. NiO particle size of the HTC catalysts in the oxidic state as a function of loading.

dominant (111) surface planes, the structure of the support surface should match the NiO(111) plane. θ-Al₂O₃ has a monoclinic structure and the oxygen ions are arranged in a distorted cubic closed packed array [20]. The Al–O distance is 1.91 Å and the (111) plane of the oxygen array of θ-Al₂O₃ (denoted as θ-Al₂O₃(111) hereafter) has a similar closed packed oxygen structure as NiO(111), but with shorter O–O distance, 2.70 versus 2.95 Å, respectively. Thus, it may be possible that the NiO particles and the θ-Al₂O₃ have a closed packed oxygen layer in common. This would explain the shorter Ni–O distance of the supported NiO particles.

Figure 8 shows possible structures of the NiO particles on the Al₂O₃ support. It is assumed that the Ni^{2+} cations are positioned above an Al^{3+} vacancy of the Al₂O₃(111) surface, because no nearest Ni–Al contribution and only a second nearest Ni–Al contribution were observed. Below 4.5 wt%, the particles consist of one Ni layer and two O layers, and above 4.5 wt%, the particles consist of two Ni layers and three O layers parallel to the NiO(111) orientation. The structure of the second layer would be close to the bulk structure, because the distances and Debye–
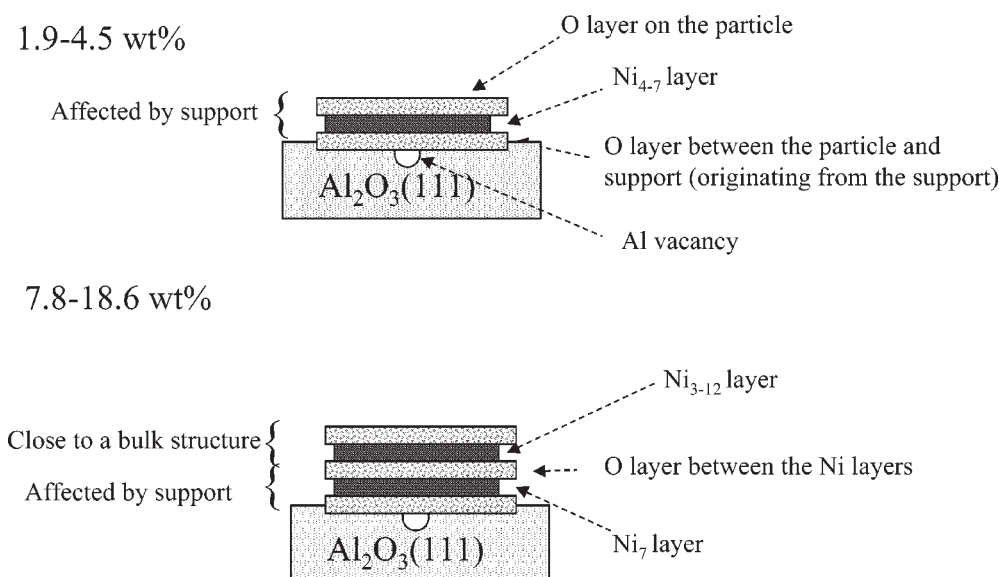
Figure 8. Possible structures of the NiO particles in the HTC catalysts in the oxidic state.

Waller factors derived by EXAFS analysis come closer to those of bulk NiO with increasing particle size and because the distance between two Ni layers is close to the bulk value. On the other hand, the structure of the first layer is affected by the support and is highly distorted. Ni–O distances are shorter than the bulk value by 0.04 Å and the Debye–Waller factor of the nearest Ni–Ni contribution is much larger than the value of bulk NiO. The average of the nearest Ni–Ni distance was almost the same as the bulk value, even when the Ni–O distance is shorter. However, the large Debye–Waller factor suggests that the distance has a wide distribution, which implies that the Ni cations cannot occupy a comfortable position and that they are statistically distorted. The fact that all Ni cations are surrounded by 6 oxygen anions suggests that there is an excess of oxygen anions. A temperature programmed reduction of these samples showed that 1.5 oxygen per nickel cation were removed during reduction, which also suggests an excess of oxygen (1). According to the models shown in table 8, the number of oxygen atoms surrounding the Ni cations is still larger than that of the removed oxygen during reduction, which suggests that the oxygen atoms between the support and particles may originate from the Al$_2$O$_3$ support and that some of the oxygen atoms surrounding the particles may exist as OH groups to compensate for the charge.

4.2. Reduced state

XANES was used to estimate the proportion of reduced Ni in the reduced samples. As shown in figure 5 and table 5, the fit was perfect. The sum of the coefficients of the reduced and the oxidic state was close to unity and the residual was small. It is obvious that the statistical error from the XANES analysis (smaller than 1%) is much smaller than that from EXAFS (ca. 20%). However, the systematic error in the XANES analysis should also be taken into account. The references used to deconvolute the XANES spectra should have a similar structure as the sample and should either be completely oxidised or reduced. The size of the Ni particles in the HTC-400 samples in the reduced state (HTC-400(r)) is close to that in the samples HTC-1.9, HTC-4.5, HTC-100 and HTC-200, as discussed in the following section. Unfortunately, we have no guarantee that HTC-400(r) is completely reduced. An alternative would be to use the Ni foil as reference compound. However, the fits of the XANES spectra with the Ni foil as reference for the reduced state were worse than that with HTC-400(r) as reference, and the result did not agree with the coordination number of the Ni–O of the unreduced Ni cations in the reduced state. XANES of small metal particles may well be different from that of bulk Ni and the use of XANES of a Ni foil as reference for that of small metal particles may cause a systematic error whose magnitude cannot be estimated. Even if it cannot be guaranteed that HTC-400(r) is fully reduced, at least 90% of the nickel will be reduced, because no Ni–O contribution was observed and the first peak of the Fourier-transformed $k \cdot \chi(k)$ could be fitted very well with a Ni–Ni contribution only. Therefore, the maximum systematic error will be about 10%, which means that the real coordination numbers of the metal particles may be larger than the calculated values by ca. 10%.

As the coordination number of the first shell is only weakly sensitive to the particle size (see the following section), the 10% error in the CN may cause a large error in particle size. However, as the CN's of the third and fourth shells are quite sensitive to the particle size, a 10% error in these CN's will not cause a large error in the particle size. In the following discussion, the proportion of reduced Ni is calculated from the XANES analysis. As discussed above, this means that the real particle sizes may be slightly larger than the sizes estimated in the following section.

Figure 9 shows CN's of the 1st–6th shells for spherical fcc Ni particles as a function of particle size. The slope of
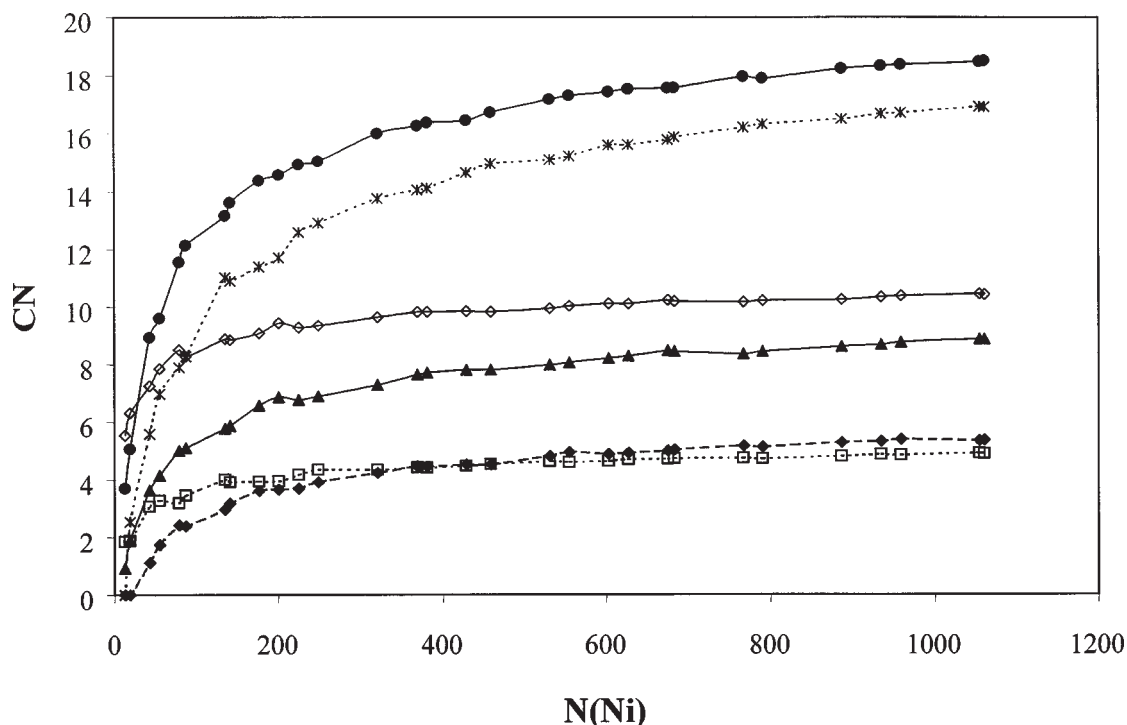
Figure 9. Coordination numbers of the 1st–6th shells for spherical Ni particles as a function of particle size. (◊) First shell, (□) second shell, (●) third shell, (▲) fourth shell, (∗) fifth shell, and (◆) sixth shell.

Table 9
Ni particle size calculated from the CN's of the first, third and fourth shells of metallic Ni–Ni.

Catalyst	Particle size[a] (number of Ni atoms) calculated from		
	First shell	Third shell	Fourth shell
HTC-1.9	62 (36–179)	34 (12–81)	22 (0–108)
HTC-4.5	78 (50–192)	47 (24–100)	35 (7–121)
HTC-100	109 (52–198)	78 (40–181)	68 (21–295)
HTC-200	120 (72–174)	75 (41–146)	73 (30–254)
HTC-400	126 (75–181)	86 (53–205)	102 (35–355)
HTC-500	302 (186–516)	175 (84–463)	170 (63–665)

[a] Values before parentheses are average values and values in parentheses are lower and upper limits.

each line became zero with increasing particle size, which means that the upper limit of the particle size contains a large error. Especially, the CN of the first shell is almost insensitive to the particle size for particles containing more than 200 Ni atoms (denoted as Ni_{200}). The curves of CN against particle size for half spherical particles are almost the same as those for spherical particles. Therefore, one cannot determine the shape of the particle from the coordination number if the particle is spherical or half spherical. Table 9 shows particle sizes estimated from the CN's of the first, third and fourth shells assuming homogeneous and spherical particles. Although the CN's of the first shells are more accurate than those of the third and fourth shells, the errors in the particle size calculated from the first shell are comparable to those calculated from the third and fourth shells, because the CN's of the third and fourth shells are more sensitive to particle size than the CN's of the first

shell. The particle size calculated from the first shell is always larger than those calculated from the third and fourth shells. The same tendency holds for a half spherical particle. This may come from the particle size distribution. The large difference between the particle sizes calculated from the first shell and from the third and fourth shells may mean a wide particle size distribution. Figure 10 shows the average and the standard deviation of the particle size assuming a spherical particle and a Gaussian distribution as a function of Ni loading. The particle sizes above 7.8 wt% can be fitted by a Gaussan distribution, but those below 4.5 wt% cannot. The average particle size between 7.8 and 15.6 wt% is $Ni_{70–100}$ with a narrow distribution. The average particle size at 18.6 wt% is Ni_{230} with a wide distribution. The particle size is insensitive to the loading in a wide range (7.8–15.6 wt%) and increased dramatically above 15.6 wt%. There are two possibilities to explain the particle size. One is that the difference of the particle size originated from the difference of the particle size in the oxidic state. The shape of the lines in figures 7 and 10 are similar to each other and the particle size of the reduced Ni is approximately ten times larger than that of the oxidic state. It suggests that the reduced Ni particles are produced by about 10 oxidic particles and that the way of particle growth does not depend on the particle size very much. Another explanation is that $Ni_{70–100}$ particles may be in a metastable state and an activation barrier may exist for further growth. In the range of 7.8–15.6 wt%, the particle size of the reduced Ni is almost insensitive to the loading while the particle size of the oxidic Ni was slightly increase with loading. When the activation barrier is overcome, the par-
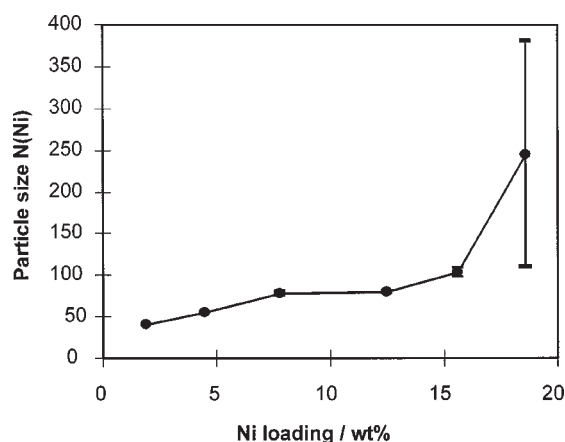
Figure 10. Particle size of the HTC catalysts in the reduced state as a function of loading, assuming spherical particles and a Gaussian distribution. (●) denotes the average particle size and the length of the bar denotes the standard deviation of the particle size distribution.

ticles grow suddenly and the particle distribution is large. We cannot exclude one of these possibilities, because the particle size calculated from the coordination number contains a substantial error.

In the above discussion, the particles were assumed to be spherical. As the CN's are insensitive to the particle shape, there is no direct evidence for this assumption. However, several results suggest a weak interaction between the particles and the support, and this should lead to spherical particles. The distance and the Debye–Waller factor of the first shell agree with that of a molecular dynamics (MD) simulation assuming free particles [12–14,21]. If the interaction between the particle and the support is strong, the distance and the Debye–Waller factor do not agree with the MD simulation of a free particle.

The possibility that the Ni–O contribution in the reduced samples is due to the direct coordination of nickel metal atoms in the Ni–Al₂O₃ interface by oxygen atoms of the support is excluded, because the XANES of the reduced sample could be reproduced by a simple linear function of oxidic and reduced state. The Ni–O contribution may be attributed to unreduced Ni cations. The short Ni–O distance (2.0 Å) suggests that such cations have migrated into the Al₂O₃ support, or are located in an unusual site.

The number of Ni atoms in the supported NiO particles is 4–22 and that of the metallic Ni particles is 40–240. The ten times larger particle size of the metallic particles means that the Ni particles grow during reduction. The strong interaction between NiO particles and support and the weak interaction between Ni metal particles and support suggest that the small NiO particles were reduced first and then diffused together.

4.3. Passivated state

The number of Ni atoms in the metallic kernels in the passivated samples were calculated to be 15–25, 30–40, 15–25, and 40–60 for HTC-100(p), 200(p), 400(p), and 500(p), respectively, from the corrected CN and figure 9.

The calculation showed that the size of the kernels was small. Those of the HTC-100(p), HTC-200(p) and HTC-400(p) samples are similar, while that of HTC-500(p) is slightly larger.

The possibility can be excluded that only exceptionally large particles have metallic kernels and that most particles are oxidised completely. Because, if this would be the case, the size of the kernels should be much larger or the proportion of the metallic nickel should be much smaller than the observed values. For instance, the number of Ni atoms in the kernel and in the whole particle of the HTC-400 sample is estimated to be 20 and 103, respectively, from the Ni–Ni CN's and figure 9. Hence, the proportion of metallic Ni is 20/103 = 0.19. This value agrees with the proportion of reduced Ni (19%) observed by XANES. Thus, the result suggests that the particles are passivated rather homogeneously.

The thickness of the oxide layer can be estimated from the sizes of the whole particles and the kernels. The diameters of the Ni₁₀₃ particle and Ni₂₀ kernel are 15 and 10 Å, respectively, and since the thickness of one Ni monolayer is 2.5 Å, this means that only one Ni layer was oxidised during passivation. As the proportion of surface Ni is large, even the oxidation of only one layer results in 81% oxidised Ni.

The Ni–O distance was shorter and the Debye–Waller factors of the Ni–O and Ni–Ni(o1) contribution were larger than those of bulk NiO. These differences may come from an unusual morphology of the NiO monolayer surrounding the metallic kernels. If the majority of the Ni particles were oxidised completely to big NiO particles, the structure parameters would be close to those of bulk NiO. The slight difference of the structural parameters suggests that the NiO particle (or domain) in the passivated state is small and surrounding the metallic Ni kernel.

5. Conclusions

The quantitative higher shell analysis provides detailed information about the shapes and sizes of the Ni and NiO particles on the Al₂O₃ surface in the oxidic, reduced, and passivated states. It also provides information about the interaction between the particles and the support. Such information cannot be obtained from a conventional first shell analysis.

In the oxidic state, the analysis of the Ni–Ni(o1) and Ni–Ni(o2) contributions provided quantitative information about the shape and size of the NiO particles and the interaction with the support. Nickel cations were present in small NiO particles with predominant (111) planes. The particle size increased with Ni loading. The particles were composed of one Ni layer accompanied with two oxygen layers below and at 4.5 wt%, and two or three Ni layers above this loading. The layers contacting the support were affected by the support and the structure was highly distorted. On the other hand, the structure of the other layers was close to the bulk structure.

In the reduced state, the particle size distribution was obtained from the Ni–Ni(m1), Ni–Ni(m3), and Ni–Ni(m4) contributions. The number of Ni atoms in the reduced particle was smaller than 100 below 15.6 wt% Ni loading with narrow distribution. The particle size was suddenly increased above this loading and widely distributed. The calculated coordination numbers of 1st–6th shell for spherical and half spherical particles were quite similar to each other. As a result, the morphology of the metal particle cannot be determined from the coordination number, directly. Ni–Ni distances and corresponding Debye–Waller factors of the particles are similar to the bulk values, which implies a weak interaction between the support and the particles. Hence, the Ni particle could be spherical because of the weak interaction.

In the passivated state, the size of the metal kernel and the thickness of the oxide skin were evaluated from the Ni–O, Ni–Ni(m1) and Ni–Ni(o1) contributions. Ni$_{20-40}$ kernels remained reduced and covered by one layer nickel oxide. The quantitative analysis suggest that most of the particles have metallic kernels and one layer oxide skins rather homogeneously. The possibility can be excluded that only exceptional large particles have metallic kernels and most of the particles were fully oxidised.

References

[1] J.P. Janssens, A.D. van Langeveld, R.L.C. Bonné, C.M. Lok and J.A. Moulijn, to be published.

[2] R. Prins and D.C. Koningsberger, in: *X-ray absorption: Principles, Applications, Techniques of EXAFS, SEXAFS, and XANES*, eds. D.C. Koningsberger and R. Prins (Wiley, New York, 1988) ch. 8.

[3] J.C.J. Bart and G. Vlaic, Adv. Catal. 35 (1987) 1.

[4] K.O. Hodgson, B. Hedman and J.E. Penner-Hahn, eds., *EXAFS and Near Edge Structure III* (Springer, Berlin, 1984) part IV.

[5] J.J. Rehr and R.C. Albert, Phys. Rev. B 41 (1990) 8139.

[6] M. Vaarkamp, I. Dring, R.J. Oldman, E.A. Stern and D.C. Koningsberger, Phys. Rev. B 50 (1994) 7872.

[7] G.G. Li, F. Bridges and C.H. Booth, Phys. Rev. B 52 (1995) 6332.

[8] S.M.A.M. Bouwens, R. Prins, V.H.J. de Beer and D.C. Koningsberger, J. Phys. Chem. 94 (1990) 3711.

[9] S.M.A.M. Bouwens, J.A.R. van Veen, D.C. Koningsberger, V.H.J. de Beer and R. Prins, J. Phys. Chem. 95 (1991) 123.

[10] R.G. Leliveld, A.J. van Dillen, J.W. Geus and D.C. Koningsberger, J. Catal. 165 (1997) 184.

[11] B.J. Kip, F.B.M. Duivenvoorden, D.C. Koningsberger and R. Prins, J. Catal. 105 (1987) 26.

[12] B.S. Clausen, L. Gråbæk, H. Topsøe, L.B. Hansen, P. Stoltze, J.K. Nørskov and O.H. Nielsen, J. Catal. 141 (1993) 368.

[13] L.B. Hansen, P. Stoltze, J.K. Nørskov, B.S. Clausen and W. Niemann, Phys. Rev. Lett. 64 (1990) 3155.

[14] B.S. Clausen, H. Topsøe, L.B. Hansen, P. Stoltze and J.K. Nørskov, Catal. Today 21 (1994) 49.

[15] P.S. Kirlin, F.B.M. van Zon, D.C. Koningsberger and B.C. Gates, J. Phys. Chem. 94 (1990) 8439.

[16] J.B.A.D. van Zon, D.C. Koningsberger, H.F.J. van 't Blik and D.E. Sayers, J. Chem. Phys. 82 (1985) 5742.

[17] S.I. Zabinsky, J.J. Rehr, A. Ankudinov, R.C. Albers and M.J. Eller, Phys. Rev. B52 (1995) 2995.

[18] A.L. Ankudinov, Ph.D. thesis, University of Washington (1996).

[19] A.J. Dobson, *An Introduction to Generalized Linear Models* (Chapman and Hall, London, 1990).

[20] W.B. Pearson, ed., Structure Reports 24 (1968) 305.

[21] L.B. Hansen, P. Stoltze and J.K. Nørskov, Phys. Rev. B 64 (1990) 3155.

[22] A.J.C.W. Wilson, ed., Structure Reports 11 (1951) 254.

[23] J. Donohue, *The Structure of the Elements* (Wiley, New York, 1974).